On the enhanced creep performance in Ti6246 achieved through Laser Powder Bed Fusion (LPBF) processing

Prince Valentine Cobbinah[a*], Sae Matsunaga[a], Yoshiaki Toda[b], Ryosuke Ozasa[c], Takuya Ishimoto[c,d], Takayoshi Nakano[c], Yoko Yamabe-Mitarai[a**]

[a]Department of Advanced Materials Science, Graduate School of Frontier Sciences, The University of Tokyo, 5-1-5 Kashiwanoha, Kashiwa, Chiba 277-8561, Japan

[b]Center for Basic Research on Materials, National Institute for Materials Science, 1-2-1 Sengen, Tsukuba, Ibaraki, 305-0047, Japan

[c]Division of Materials and Manufacturing Science, Graduate School of Engineering, Osaka University, 2-1 Yamadaoka, Suita, Osaka 565-0871, Japan

[d]Aluminium Research Center, University of Toyama, 3190 Gofuku, Toyama 930-8555, Japan

*Corresponding authors' email: p.cobbinah22s@ams.k.u-tokyo.ac.jp

**Corresponding authors' email: mitarai.yoko@edu.k.u-tokyo.ac.jp

Abstract

The high susceptibility of the Ti-6Al-2Sn-4Zr-6Mo wt.% (Ti6246) alloy to microstructural changes stands as a challenge when processed by the laser powder bed fusion (LPBF) technology. However, leveraging the capabilities of the LPBF process to successfully control the microstructure (and/or crystallographic texture) of the Ti6246 could improve mechanical properties, particularly at elevated temperatures. In this study, the creep performance (at 500 °C) of Ti6246 fabricated from three different LPBF processing conditions and heat-treated (HT) at 885 °C were investigated. In the as-built state, all the LPBFed-Ti6246 exhibited columnar microstructures with crystallographic lamellar-like microstructure (CLM), a near single crystal-like microstructure (SCM), and polycrystalline microstructure (PCM) textures, respectively. At low applied stresses (100 – 300 MPa), diffusional creep was the dominant deformation mechanism and its resistance depended on grain size. The reference β-forged-HT Ti6246, characterized by large equiaxed grains, exhibited the lowest strain rate compared to the columnar microstructure of SX1 (CLM)-HT, SX2 (SCM)-HT, and SX3 (PCM)-HT. Conversely, dislocation slip governed deformation at high applied stresses (400 - 580 MPa) and its efficacy

depended on the α/β interfaces in the microstructures. Disjointed columnar grains in SX1 (CLM)-HT and the deformation of the polycrystalline grains in SX3 (PCM)-HT indicated that the melt pool boundaries were unstable in the LPBFed-Ti6246. SX2 (SCM)-HT exhibited the longest creep life due to the relatively stable melt pool boundaries and the near <001> SCM crystallographic texture parallel to the applied stresses. Shallow dimples, cleavage facets, and the observation of laser scan tracks characterized the fracture surfaces of the LPBFed-Ti6246. These indicated that failure occurred by intergranular fracture resulting from the formation of creep voids at the melt pool boundaries.

Keywords: LPBF; columnar microstructure; melt pool boundary stability; creep voids; diffusion creep, dislocation creep

Introduction

The Ti-6Al-2Sn-4Zr-6Mo wt.% (Ti6246) alloy is an α + β alloy classified under the same group as the Ti-6Al-4V wt.% (Ti64) alloy. One primary advantage of the Ti6246 alloy over the Ti64 is its high susceptibility to microstructural changes, which allows a wide heat treatment processing window. However, this high sensitivity of the microstructure of the Ti6246 could pose a challenge when processed using the laser powder bed fusion (LPBF). This is because the LPBF is an additive manufacturing (AM) process that involves local melting, rapid cooling, remelting of already solidified layers, and a repeated heating cycle during fabrication [1]. This repeated cycle is well known to influence the microstructures of LPBF processed parts significantly [2].

So far, few studies on Ti6246 have involved the LPBF process [3-5]. Carrozza et al. [3] varied input energy density and achieved fully dense Ti6246 using the LPBF process. The authors also observed prior-β grains of columnar morphology and a martensitic microstructure, with higher input energy density resulting in finer α′′needles in the as-built samples. Furthermore, the as-built samples exhibited substantial ductility but low yield strength. Conversely, post-heat treatments markedly increased the strength of the LPBFed-Ti6246 at the expense of ductility [4]. Peng et al. [5] also observed the α′′martensitic microstructure in LPBFed-Ti6246. Heat treatment at 650 °C significantly improved the hardness of the samples owing to the decomposition of the

α″phase to the α and β phases. As reported in the studies mentioned above as well as many other studies on titanium (Ti) α + β alloys such as Ti64 [6, 7], mechanical behavior primarily depends on formed microstructural features such as phase morphology, the type of precipitate that forms, precipitate size, and distribution.

At elevated temperatures, mechanical behavior is also influenced by the synergistic effects of temperature and applied stress on the Ti alloy. Creep resistance is an example of a high-temperature mechanical property strongly desired in structural materials (e.g. Ti6246) used for aerospace applications. To the best of the authors' knowledge, no previous study has paid attention to the creep performance of Ti6246 processed by the LPBF. In our previous study [8], we optimized the LPBF process parameters over a wide range and studied their effects on the Ti6246. First, we observed the formation of α/α'phases of varying sizes depending on the LPBF process parameters. Also, the far ends of the investigated parameters i.e. samples with volumetric energy density (VED) $\geq$ 62.5 J/mm^3 formed columnar microstructures whereas VEDs $\leq$ 30 J/mm^3 formed polycrystalline microstructures. As a progress of our research, the present study evaluates the creep performance of the LPBFed-Ti6246 focusing on three different processing conditions (further details are provided in Section 2). Aside from the different microstructures, the three processing conditions were chosen because of the unique texture they exhibited. Laser power of 360 W at 600 mm/s scan speed (VED = 75 J/mm^3) produced alternating textures termed crystallographic lamellar-like microstructure (CLM) texture, 300 W at 1000 mm/s (VED = 50 J/mm^3) formed a near-single crystal-like microstructure (SCM) texture, and 180 W at 1200 mm/s (VED = 25 J/mm^3) resulted in a polycrystalline crystallographic microstructure-like (PCM) texture. This study is the first to report such unique textures for Ti6246. For further insights and comparison with the LPBFed-Ti6246, the present study also investigated the conventional β-forged Ti6246.

In all, texture is an important property determinant factor that significantly influences creep resistance. Hence serving as a strong motivation for the current study.

Materials and methods

Gas-atomized Ti-6Al-2Sn-4Zr-6Mo wt.% (Ti6246) powders with spherical morphologies served as starting powders. Rectangular samples of height, 40 mm, and width 7 mm were

fabricated using the EOS M290 M LPBF equipment (EOS GmbH, Germany). Table 1 summarizes the LPBF process conditions used.

Table 1: Ti6246 LPBF process conditions

	Process parameters				
Sample name	Laser power, P (W)	Scan speed, v (mm/s)	Hatch distance, d (µm)	Powder layer thickness, t (µm)	VED (J/mm^3)
SX1 (CLM)	360	800			75
SX2 (SCM)	300	1000	100	60	50
SX3 (PCM)	180	1200			25

The energy inputs involved in the LPBF process were quantified as volumetric energy density (VED) and defined as:

$$\text{VED (J/mm}^3\text{)} = \frac{P}{vdt}$$

Furthermore, the bidirectional scan strategy along the X-axis with no rotations in subsequent layers was used. Therefore, the scanning direction was in the XY plane, and the build direction was parallel to the YZ plane.

A Ti6246 ingot β-forged at 1000 °C was also investigated and used as a reference alloy for comparison with the LPBFed-Ti6246.

The LPBFed and β-forged Ti6246 were heat-treated (HT) at 885 °C for 1 hour and air-cooled. The samples were then machined into the "dog-bone" shape, as illustrated in Figure 1. Table 2 summarizes the gauge diameter and gauge length of the creep samples. The R-type thermocouples were attached to each sample to measure the testing temperature and the respective elongation was measured using a linear gauge. To investigate the occurring transitions of deformation mechanisms during the tensile creep test, the step creep test was performed at 500 °C starting with a 100 MPa stress in air condition. The applied stress was then increased to 200, 300, 400, 500, and 580 MPa. The tensile creep test continued until fracture occurred under 580 MPa. Furthermore, the strain rate and applied stresses were analyzed using the classic Bird-Mukherjee-Dorn equation, and the prevalent deformation mechanisms were estimated.

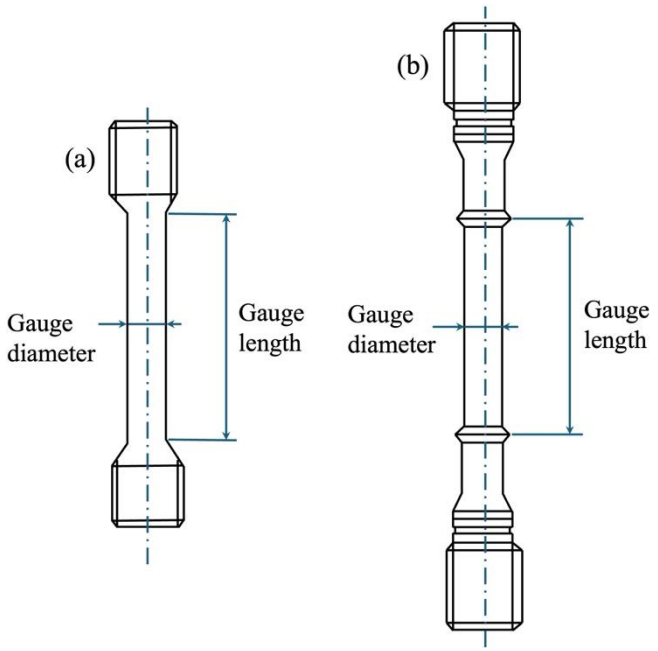

Figure 1: Schematics of "dog-bone" shape for (a) SX1 (CLM)-HT, SX2 (SCM)-HT, and SX3 (PCM)-HT and (b) β-forged-HT Ti6246 used for creep tests.

Table 2. Gauge diameter and gauge length of creep samples.

Sample name	Gauge diameter (mm)	Gauge length (mm)
SX1 (CLM)-HT	2.830	12.960
SX2 (SCM)-HT	2.832	12.991
SX3 (PCM)-HT	2.837	13.053
β-Forged-HT	6.017	30.001

The JEOL JSM-7200F scanning electron microscope (SEM) equipped with an electron backscatter diffractometer (EBSD) and backscattered electron (BSE) detector was used to characterize the microstructure of the heat-treated, cross-section, and fractured surfaces of all the tested samples. Foremost, the building directions (YZ plane) of all the heat-treated samples and their respective cross-sections after the creep testing were mounted, metallographically ground, and polished, with the final stage of polishing involving 0.05 μm colloidal silica for 10 minutes. The EBSD analysis covered minimum areas measuring 300 x 300 μm with a step size of 0.9 μm. The EBSD data was analyzed using the TSL OIM 8 software.

Results

1.1 Microstructure and texture of the as-built Ti6246

Figure 2 (a) - (c) shows the SEM-BSE images of the as-built Ti6246. The as-scanned microstructures of SX1 (CLM), SX2 (SCM), and SX3 (PCM) exhibited well-defined columnar

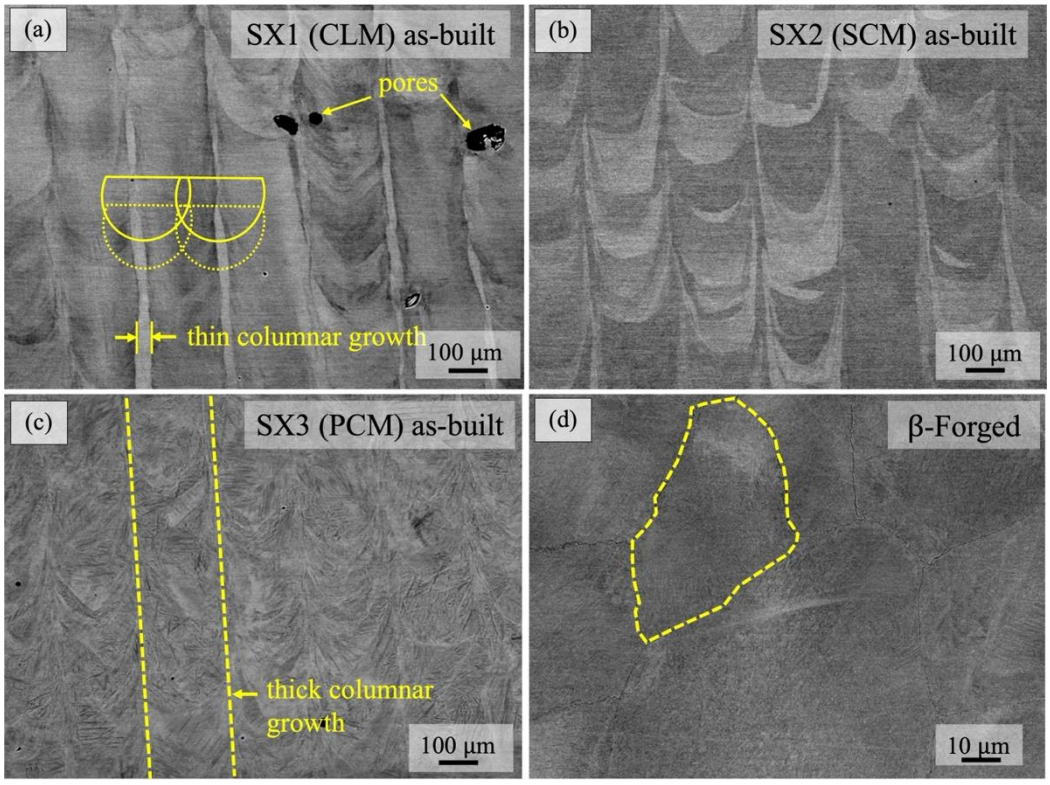

Figure 2: SEM-BSE images of the as-built LPBFed-Ti6246 (a) SX1 (CLM), (b) SX2 (SCM), (c) SX3 (PCM) observed from the build direction (YZ plane), and (d) β-forged sample.

morphologies in the build direction. Although typical of the LPBF process, the continuous and defined columnar growths observed in the present study differ from the few reported studies on LPBFed-Ti6246 [3-5]. Apart from the obvious difference in process parameters, one possible explanation could be the high laser power employed in the present study. Particularly in SX1 (CLM), the columnar growth occurred in an alternating sequence of thick and thin columnar structures, as depicted in Figure 2 (a). The thick columnar structures occurred at the overlapping ends of the melt pools whereas the thin secondary columnar structures formed and connected at the centers.

The defined continuous thick growth at the overlapping ends suggests that during the layer addition process, the localized melting sufficiently remelted the topmost parts of already solidified layers or exceeded the powder layer thickness of 60 μm promoting the epitaxial growth of existing grains. Concurrently, nucleated new grains at the overlapping ends of the new melt pools also inherited the growth direction through competitive growth leading to the columnar microstructure.

As already reported [8], the black phases in all the SEM micrographs were identified as the α/α' martensitic phase. Additionally, it is worth noting that the α'' and ω phases were not identified in any of the as-built samples. The sizes of the precipitates (α/α' phase) formed in SX1 (CLM) were observed to be extremely refined (in the nanoscale) while those formed in SX3 (PCM) were relatively coarse (microsized). In SX2 (SCM), the sizes were between those of SX1(CLM) and SX3 (PCM). The observed precipitate size differences were mainly attributed to the VEDs used for the respective builds. Readers are referred to our previous study for further insights [8]. On the other hand, the β-forged sample exhibited an equiaxed microstructure with an average grain size of 138 ± 49 μm, as depicted in Figure 2 (d). Also, the precipitated α' martensitic phase were refined and of the nanoscale.

Figure 3 shows the β-phase reconstructed EBSD IPF maps of the as-built Ti6246. In fact, it has been reported that crystallographic texture evolution in the LPBF process largely depends on the melt pool shape particularly the depth or curvature of the melt pool bottoms [9]. Analogous to the casting process, the LPBF process forms a non-homogeneous nucleation at the

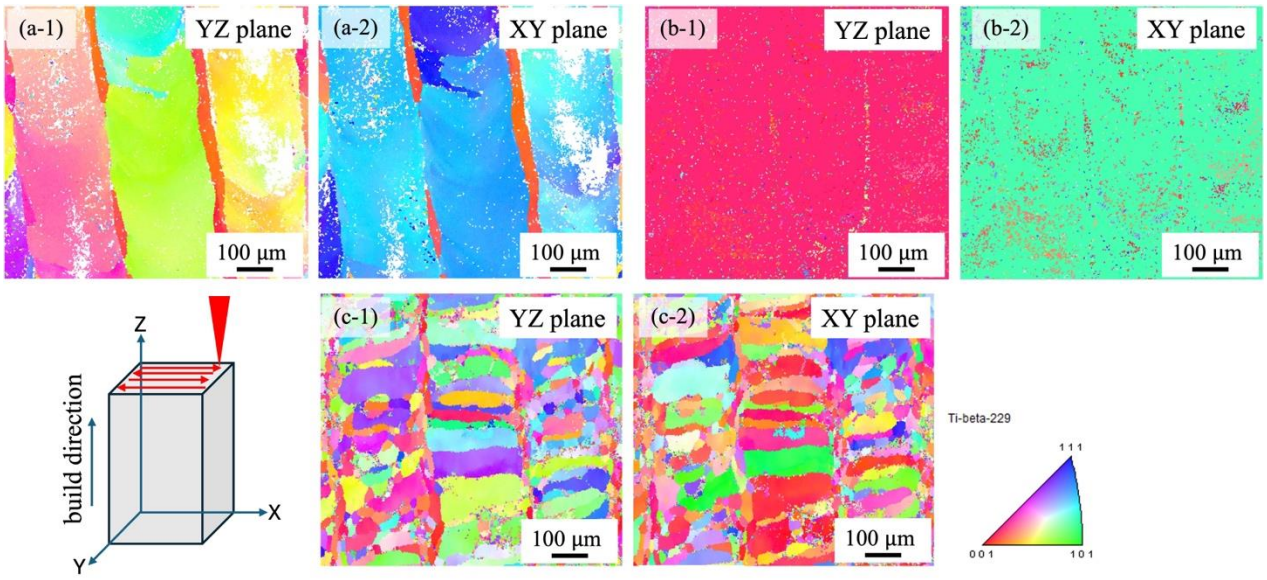

Figure 3: Reconstructed β-phase EBSD IPF maps of (a-1) and (a-2) crystallographic lamellar microstructure-like (CLM) texture in SX1, (b-1) and (b-2) near single-crystal-like microstructure (SCM) texture in SX2, and (c-1) and (c-2) polycrystalline microstructure-like (PCM) texture in SX3. (YZ plane - build direction, XY plane - scanning direction). [(c-1) is reproduced under terms of the Creative Commons CC BY 4.0 license [8]. Copyright 2024, The Authors. Published by Elsevier B.V. on behalf of KeAi Communications Co. Ltd.]

solid phase boundary at the melt pool bottom (or fusion region). The direction of heat flow is fastest perpendicular to the solid-liquid interface, with grains competitively and at the same time preferentially growing along in the opposite direction [10]. The <111> and <001> textures were observed to alternate in a lamellar-like pattern in the scanning direction (XY plane) of SX1 (CLM) fabricated with a 360 W laser power input at a scan speed of 800 mm/s. This lamellar-like orientation of crystallographic texture has been reported in other studies and is termed as crystallographic lamellar-like microstructure (CLM) texture [11]. The evolution of the CLM texture is usually attributed to the formation of deep melt pools [11]. The employed laser power input of 360 W at a slow speed (800 mm/s) combination (high energy) produced deep melt pools in SX1 (CLM) during the building process. The formed deep melt pools enhanced the epitaxial growth of grains resulting in the columnar microstructure and promoted the inheritance of the existing crystallographic orientations from one layer to another. According to Thijs et al. [12], builds involving high-energy inputs are more likely to result in the formation of the <111> texture. On the other hand, the <001> texture is seen to have evolved at the center of the melt pools where

energy is highest during the LPBF process. Thus, the <001> texture preferentially and continuously grew at the center of the connecting melt pools along the build direction (YZ plane) owing to the downward heat flow.

Similarly, a near <001> and <110> single crystal-like microstructure (SCM) texture formed in the build (YZ plane) and scanning (XY plane) directions of SX2 (SCM) (300 W, 1000 mm/s) as presented in Figures 3 (b-1) and (b-2), respectively. The columnar microstructure, as evident in Figure 2 (b), suggests relatively deep melt pools also formed in SX2 (SCM). Gokcekaya et al. [13] postulated that when deep melt pools form with the solidification front almost horizontal at the melt pool centerlines, two easy-growth directions perpendicular to each other from the melt pool sides and center occur resulting in the <001> cubic texture evolution along the build direction. From another perspective, the evolution of the <001> texture along the build direction may be attributed to the fixed laser scanning direction employed. Without any rotations, the bidirectional scanning along the X-axis resulted in a homogeneous thermal flux in each melt pool (and layer), ultimately promoting grain preferential growth in the <001> direction. Similar texture has been reported for face-centered cubic (fcc) based alloys such as nickel-based superalloys and stainless steels [9, 11, 14].

Although the SEM-BSE image of SX3 (PCM) showed a columnar microstructure, the EBSD analysis revealed the polycrystalline crystallographic microstructure (PCM) texture formed in both the build (YZ plane) and scanning (XY plane) directions, as shown in Figure 3 (c-1) and (c-2) respectively. Unlike SX1 (CLM) and SX2 (SCM), the curvature of the bottom of the melt pools formed in SX3 (PCM) (180 W, 1200 mm/s) significantly decreased owing to both the low laser power input and the fast scan speed. This combination of process parameters prevented the epitaxial growth of grain at the fusion region (or melt pool bottom) and the consequent inheriting of previous crystal orientations. Thus culminating in the observed randomly oriented small grains in SX3 (PCM).

1.2 Microstructure of the heat-treated LPBFed-Ti6246

Figure 4 shows the SEM-BSE images of the heat-treated (HT) LPBFed and β-forged Ti6246. As expected, the α' martensitic phases coarsened and decomposed to the α phase. This is because, generally, the decomposition of the α' martensitic phase to the α phase is diffusion-driven, requiring elevated temperature and sufficient time. Foremost, the micrographs provided

insight into the locations of the precipitated martensitic phase before heat treatment. The α phase, therefore, were found within the columnar structures and boundaries (longitudinal boundaries) and the melt pool boundaries. Similarly, in the β-forged-HT Ti6246, the α phase were located in the equiaxed grains as well as at the grain boundaries. This is in good agreement with available literature on the Ti6246 [15, 16].

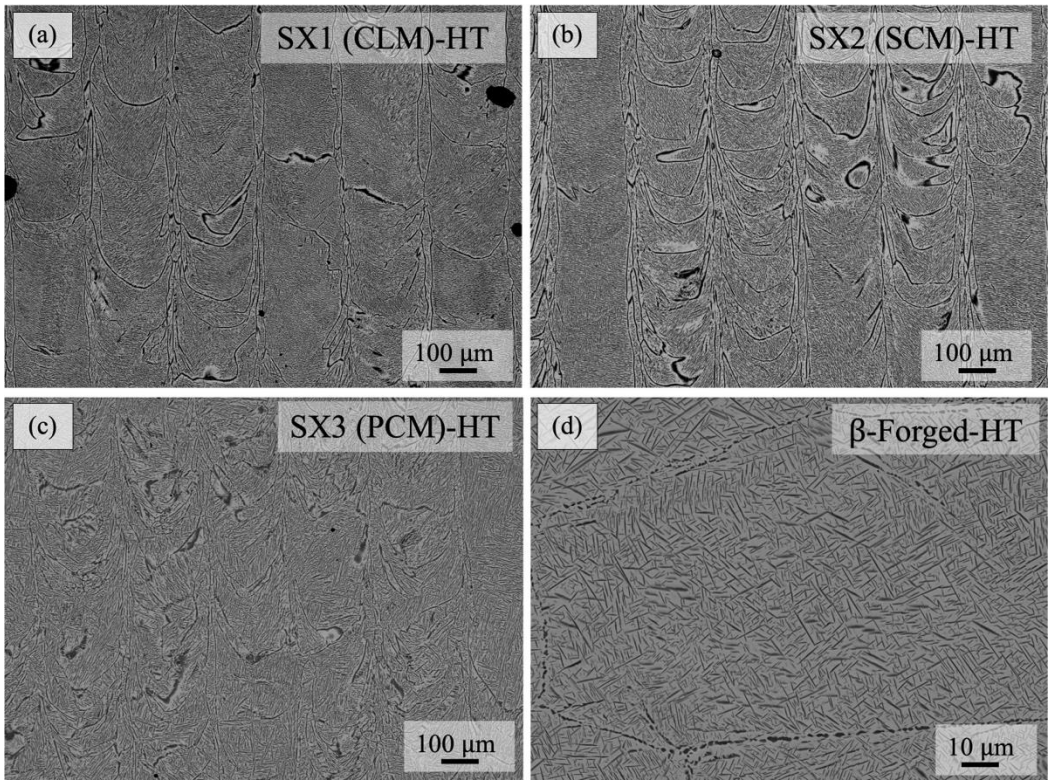

Figure 4: SEM-BSE images of the heat-treated (HT) LPBFed-Ti6246 (a) SX1 (CLM), (b) SX2 (SCM), (c) SX3 (PCM) observed from the build direction (YZ plane), and (d) β-forged sample.

Figure 5 presents the volume fraction and average lengths of the α phase in the LPBFed and the β-forged Ti6246 after HT. The volume fraction of the α phase in SX2 (SCM)-HT and SX3 (PCM)-HT was about the same (~ 40) after heat treatment. Conversely, the measured average lengths increased from 3.78 µm in SX1 (CLM)-HT to 7.03 µm in SX3 (PCM)-HT. The β-forged-HT Ti6246, on the other hand, exhibited the least α volume fraction (27), but the measured average length (5.5 µm) was between those of SX2 (SCM)-HT and SX3 (PCM)-HT.

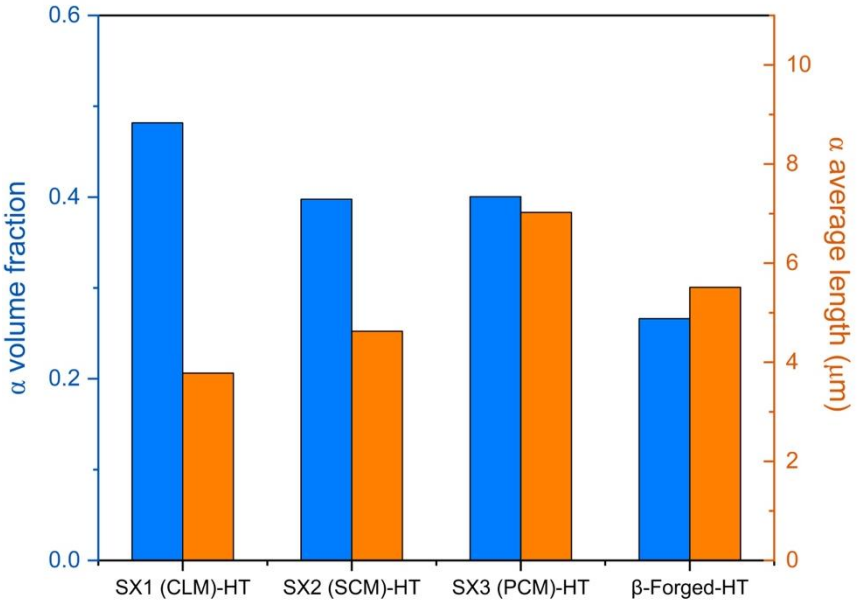

Figure 5: α phase volume fraction and average length (μm) in the LPBFed and the β-forged Ti6246 after heat treatment (HT) at 885 °C for 1 hour and air cooled.

1.3 Creep behavior of the heat-treated LPBFed and β-forged Ti6246

Figure 6(a) shows the LPBFed and β-forged Ti6246 creep curves. Compared to the HT LPBFed-Ti6246, the β-forged-HT Ti6246, with an equiaxed microstructure, exhibited the least strain till fracture. Despite the similarity in the microstructures of LPBFed-Ti6246, their creep lives varied, in the range of 380 – 440 hours. Overall, SX2 (SCM)-HT had the longest creep life. Therefore, to determine the deformation mechanisms in the respective samples, step creep tests were performed. Figure 6(b) shows the respective creep curves of the step creep tests. The steady-state strain rate

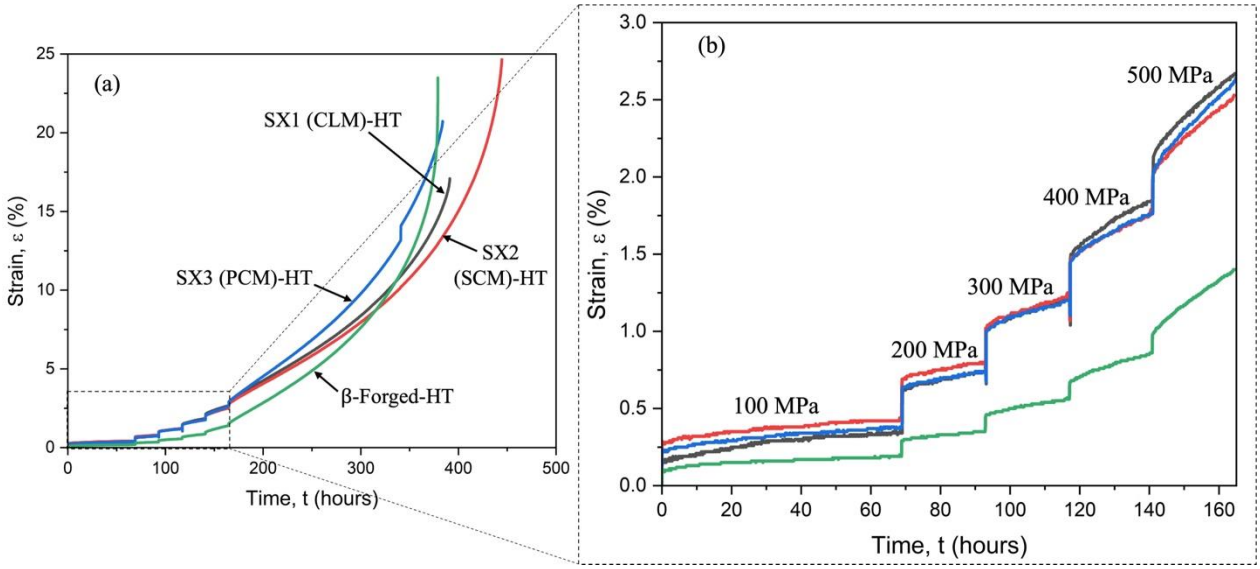

Figure 6: (a) Overall and (b) step creep curves of SX1 (CLM)-HT, SX2 (SCM)-HT, SX3 (PCM)-HT, and β-Forged-HT Ti6246 at 500 °C.

($\dot{\varepsilon}$) usually varies with the applied stress (σ), the absolute temperature (T), and the grain size of the material (d_g) through a relationship that can be expressed in the form of Eq. 1 [17].

$$\dot{\varepsilon} = \dot{\varepsilon}_o \frac{GV_a}{k_o T} \left(\frac{b}{d_g}\right)^p \left(\frac{\sigma}{G}\right)^n \frac{D}{b^2} \quad (1)$$

where $\dot{\varepsilon}$, G, V_a, k, b, D, p, and n represent the strain rate independent of temperature and stress, shear modulus, atomic volume, Boltzmann's constant, Burgers vector, diffusion coefficient (= D_0 exp ($-Q/RT$), where D_0 is a frequency factor, Q is the activation energy and R is the gas constant), the inverse grain size exponent, and apparent stress exponent, respectively. In the present study, the grain size (i.e. melt pool size) and testing temperature do not change, thus the steady-state strain rate ($\dot{\varepsilon}$) can be considered as a function of the applied stress (σ). Therefore, Eq. 1 can be further expressed as:

$$\log \dot{\varepsilon} = \log A + n \log \sigma \quad (2)$$

$$\text{where } A = \dot{\varepsilon}_o \frac{GV_a}{k_o T} \left(\frac{b}{d_g}\right)^p \frac{D}{b^2}$$

In general, the deformation mechanisms in metallic alloys that control high-temperature creep include diffusional creep [18, 19], grain boundary or interface sliding [20, 21], dislocation glide and climb [22, 23], and viscous dislocation glide controlled by dragging of solute atoms or by jogs [24, 25].

One method of knowing which deformation mechanism dominates is by determining the values of the apparent stress exponent (n). The gradient from plotting log $\dot{\varepsilon}$ vs log σ, is used to determine the apparent stress exponent (n) as depicted in Figure 7. For each applied stress, the

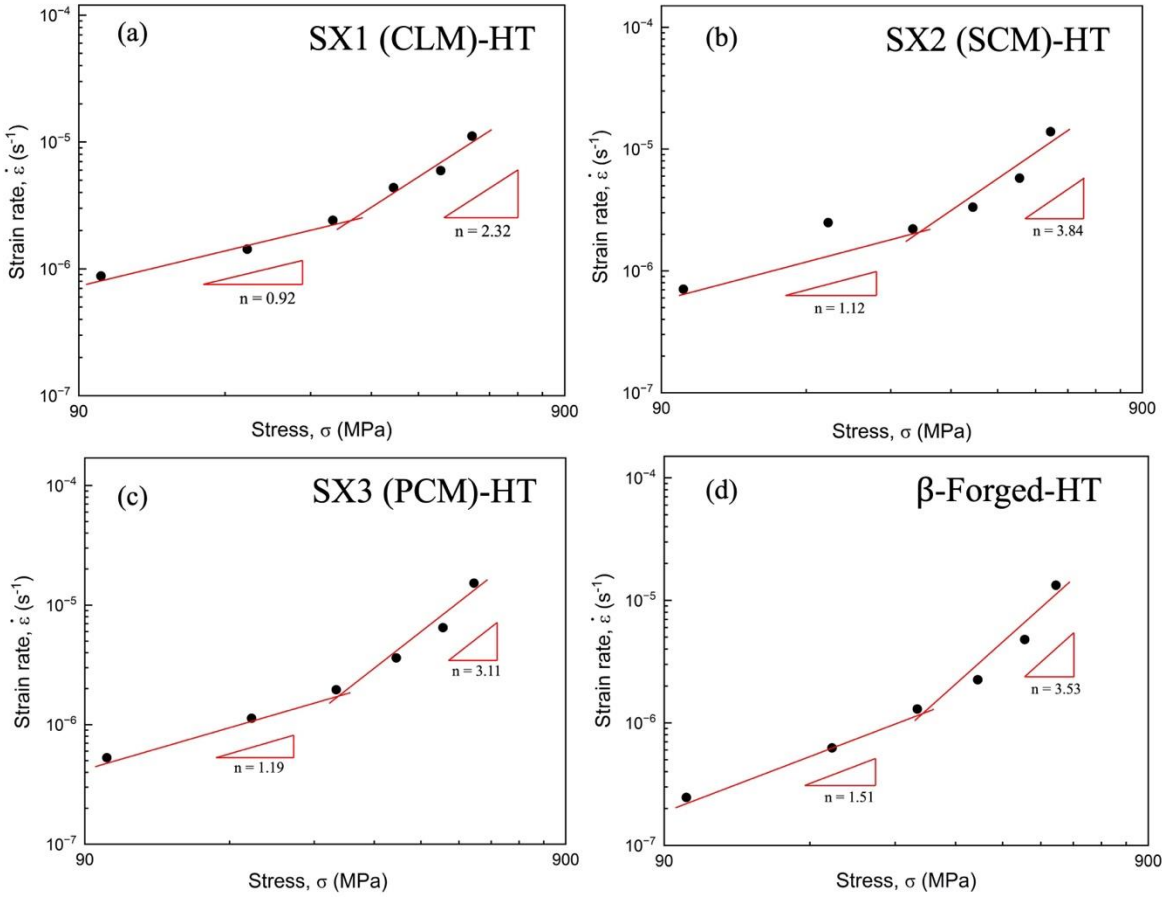

Figure 7: Dependence of steady-state creep on applied stress at 500 °C in (a) SX1 (CLM)-HT, (b) SX2 (SCM)-HT, (c) SX3 (PCM)-HT, and (d) β-Forged-HT Ti6246.

minimum creep rate value was determined from the steady-state regime where the creep curve exhibited a distinct plateau. As Figure 7 shows, the values of n fall along two different lines depending on the applied stresses in all the HT LPBFed and the β-forged Ti6246. The apparent stress exponent (n) increased rapidly when the applied stresses exceeded 300 MPa. This breakaway indicates a transition in the occurring deformation mechanisms. It is well-established that when $n \cong 1$, the dominant creep process is associated with the Nabarro-Herring-Coble creep (i.e. diffusion creep) mechanisms whereas when $n \cong$ 2-3 the grain boundary sliding mechanism dominates. Above 3, dislocation slip is the dominant deformation mechanism.

The cross-section of each sample was investigated after fracture to understand the effect of the various microstructures on the observed creep behaviors. The microstructures of the cross-section of the samples after the creep tests are shown in Figure 8. It was observed that the grains in SX1 (CLM)-HT changed from long pronounced columnar structures to disjointed columnar structures

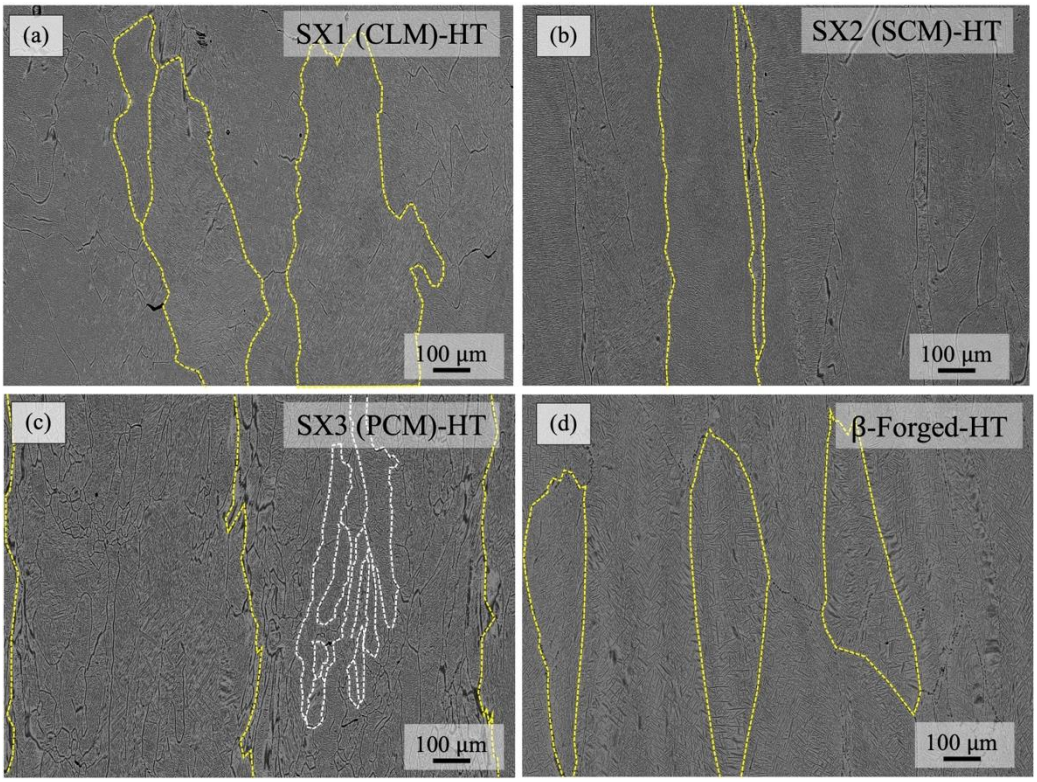

Figure 8: SEM-BSE images of the cross-sections of (a) SX1 (CLM)-HT, (b) SX2 (SCM)-HT, (c) SX3 (PCM)-HT, and (d) β-Forged-HT samples after fracture. The yellow dotted lines indicate the grain boundaries. The elongated substructures were also marked with dotted lines.

(Figure 8(a)). On the other hand, samples SX2 (SCM)-HT and SX3 (PCM)-HT maintained their columnar structures parallel to the build direction as depicted in Figure 8 (b) and (c), respectively. Interestingly, the width of the columnar structures widened in SX3 (PCM)-HT from 92 µm to 268 µm. The threefold increase in the width may suggest the fusing of columnar structures and is corroborated by the formation of elongated substructures (deformed grains) noticed within the thick columnar structures. For the β-forged Ti6246, the equiaxed grains were elongated in the direction of the applied stresses as depicted in Figure 8 (d).

297 1.4 Fracture surfaces after creep tests

298 SEM secondary electron images of the fractured surfaces after the creep tests are shown in
299 Figure 9. Many shallow dimples were observed in SX1 (CLM)-HT as depicted in Figure 9 (a). A
300 closer examination of the interior of the dimples revealed the existence of rings at different
301 depths (inset of Figure 9 (a)). These rings are likely melt pool boundaries from different layers of
302 the build. The fracture surface of SX2 (SCM)-HT also exhibited similar shallow dimples as
303 noticed in
304

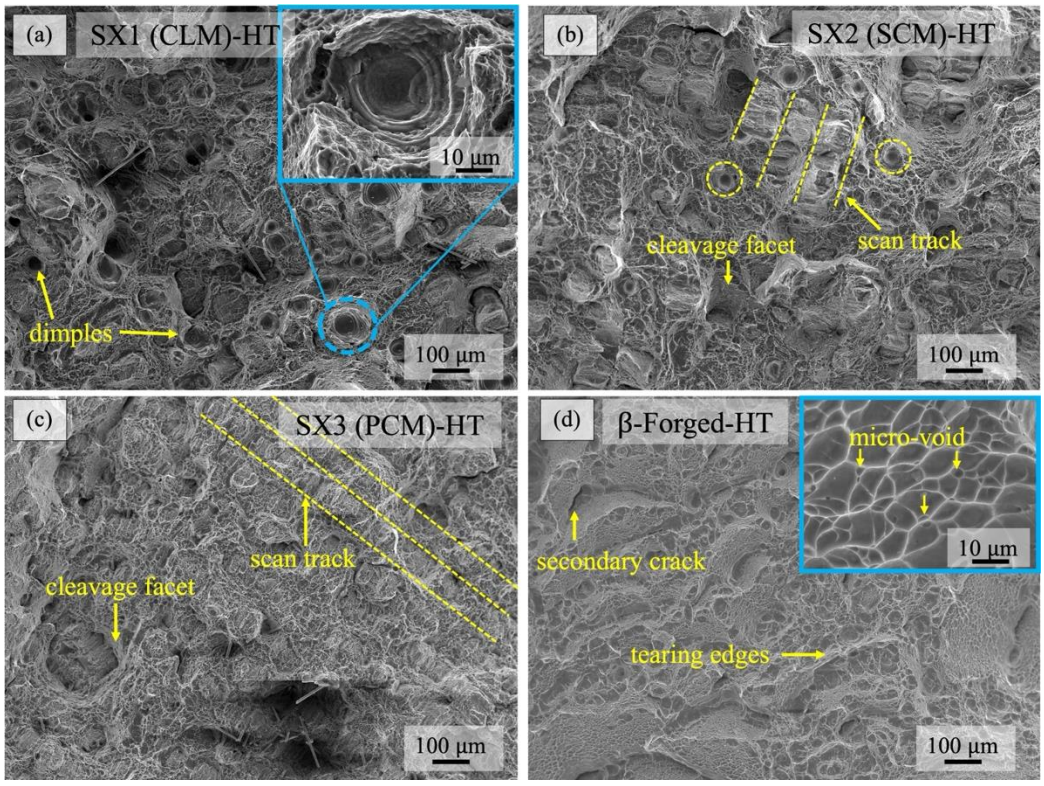

305
306 Figure 9: SEM secondary electron images of the fracture surfaces of (a) SX1 (CLM)-HT, (b)
307 SX2 (SCM)-HT, (c) SX3 (PCM)-HT, and (d) β-Forged-HT Ti6246.

308 SX1 (CLM)-HT. In addition, clear outlines of the laser scan pathways were observed as indicated
309 by the dotted lines in Figure 9 (b). This observation suggests delamination i.e. separation of
310 layers likely from the applied constant pull. Furthermore, the polycrystalline SX3 (PCM)-HT
311 showed outlines of the laser scan pathways and some cleavage facets as depicted in Figure 9 (c).
312 The β-forged-HT Ti6246 exhibited a mix of secondary cracks, tearing edges, and cleavage facets
313 (Figure 9 (d)). At high magnification, micro-voids were observed at the grain boundaries as
314 arrowed in the inset of Figure 9 (d).

Although some obvious cleavage facets and tearing edges were observed in some samples, the overall creep fracture surface morphologies of the LPBFed and β-forged-HT Ti6246 primarily indicate intergranular brittle fracture modes. Similar observations have been reported by He et al. [26] on the creep performance of LPBFed-Ti64.

Discussion

Generally, the relatively low mechanical properties of additive manufactured (AM) products are attributed mostly to defects such as pores. These pores are the vulnerable areas where cracks initiate and propagate leading to failure. However, the LPBF AM process boasts of forming fully dense products that help circumvent the effects of pores on mechanical properties, particularly at room temperature. Aside from pores, many factors can influence the mechanical properties of LPBFed products. The present study delved into uncovering and understanding the deformation mechanisms of LPBFed-Ti6246 during creep at 500 °C.

1.5 Effect of microstructural stability on creep

The apparent stress exponent (n) values for the applied stresses from 100 - 300 MPa in all the Ti6246 samples indicate the diffusional creep mechanism controlled the creep process, as shown in Figure 7. The mechanisms of diffusional creep test the stability of microstructures owing to the movement of matter. As such, it is well established that diffusional creep rate hinges on microstructural features including grain size and morphology [27]. As evident in Figure 6, the β-forged-HT Ti6246 with equiaxed grains of average size 138 ± 49 μm exhibited a lower strain rate than the columnar structures of SX1 (CLM)-HT, SX2 (SCM)-HT, and SX3 (PCM)-HT. The observed low strain rate implies that the large grain sizes of the β-forged-HT Ti6246 showed resistance to diffusional creep owing to the increased distance through which matter had to diffuse for deformation to occur. In addition, we argue that the equiaxed morphology and large grain sizes in the β-forged-HT Ti6246 presented a more stabilized microstructure because the microstructure homogenously deformed under low applied stresses. In other words, the elongation of the individual grains was directly proportional to the macroscopic elongation of the β-forged-HT Ti6246 sample (Figure 8(d)).

In the case of the HT LPBFed-Ti6246, because the columnar structures were parallel to the applied stresses, the effects of the diffusional creep manifested at the melt pool and longitudinal

grain boundaries. Although no significant differences were observed in the strain rates in SX1 (CLM)-HT, SX2 (SCM)-HT, and SX3 (PCM)-HT, the melt pool boundaries perpendicular to the applied stresses were the most vulnerable regions as a result of the nonuniform distribution of stress concentration as creep proceeded [28]. Hence microstructural stability in the HT LPBFed-Ti6246 during diffusional creep depended on the stability of the melt pool boundaries. This is because the melt pool boundaries act as conduits for atom migration during diffusional creep. One effect of the melt pool boundary instability as diffusional creep occurred, is seen in SX1 (CLM)-HT (Figure 8(a)) wherein the long pronounced columnar structures changed to disjointed columnar structures. In SX3 (PCM)-HT, the effect of the melt pool boundary instability, as already mentioned, culminated in elongated substructures (deformed grains) and the increase in the size of the columnar structures. Consistent with literature [29], diffusion enabled the melt pool boundaries in the polycrystalline microstructure of sample SX3 (PCM)-HT to slide as an accommodation mechanism. The sliding of the melt pool and longitudinal boundaries preserved the continuous deformability while avoiding microcracking during diffusion creep. On the other hand, compared to the SX1 (CLM)-HT, SX3 (PCM)-HT, and the β-forged-HT Ti6246, the microstructure of SX2 (SCM)-HT showed no noticeable changes from the mechanisms of diffusional creep. We can, therefore, infer that the melt pool and longitudinal boundaries were stable and as such efficiently resisted the diffusional deformation at the low applied stresses.

1.6 Role of the α/β interface

It is well documented that precipitates such as the α phase inhibit diffusional creep [30]. However, as the applied stresses increased above 300 MPa, the deformation mechanism in all the HT LPBFed and β-forged Ti6246 deviated from diffusional creep to dislocation slip (with $n \cong$ 2.3 (SX1 (CLM)-HT), 3.8 (SX2 (SCM)-HT), 3.1 (SX3 (PCM)-HT), and 3.5 (β-forged-HT)). As elucidated in our previous study [8], the precipitate sizes in the as-built Ti6246 were quite peculiar. Contrary to several existing studies [31, 32], the low laser power input at fast scan speed combination (fast solidification rate) used in SX3 (PCM) resulted in coarse martensitic precipitates whereas the high laser power input at slow scan speed (slow solidification rate) in SX1 (CLM) formed refined martensitic precipitates. Figure 10 compares the α-phase volume fraction and average lengths after heat treatment (HT) and creep tests at 500 °C. The volume fraction of the α phase after HT and creep tests remained nearly the same in SX1 (CLM)-HT,

SX2 (SCM)-HT, and SX3 (PCM)-HT as well as the β-forged-HT. Furthermore, the α-phase volume fraction in the

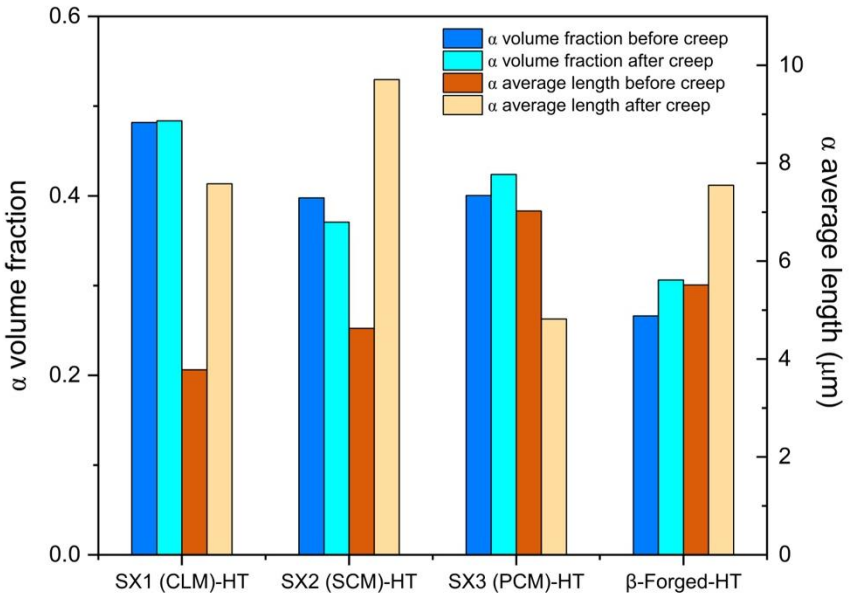

Figure 10: α phase volume fraction and average length (μm) in the HT LPBFed and the β-forged-Ti6246 before and after the creep test at 500 °C.

respective samples constituted less than 50% of the overall microstructure, indicating that the minimum creep rate at stresses greater than 300 MPa depended on the deformation of the α-phase precipitates and the β-phase matrix. Since the α-phase precipitates and the β-phase matrix exhibit different strengths, their interface experiences all the occurring local strains. During deformation, these α/β interfacial regions become barriers to dislocations, and as a result, account for the deformation resistance under high applied stresses. However, the more dislocations accumulate and interact energy increases, which simultaneously decreases the efficacy of the α/β interfacial regions. The role of the α/β interfacial regions suggest the α-phase volume fraction has a direct relation to deformation resistance at high applied stresses. This was made evident in the β-forged-HT Ti6246, where the low α-phase volume fraction culminated in a large accelerated deformation at stresses greater than 300 MPa (Figure 6(a)). Along similar lines, Ro et al. [33] after investigating several α/β Ti alloys at 500 °C, asserted that the presence of a high α-phase volume fraction tends to decrease the steady-state creep rate in good agreement with the observed deformation behavior in SX1 (CLM)-HT, SX2 (SCM)-HT, and SX3 (PCM)-HT. In all,

despite being a classic concept, the notion that the α/β interfacial regions control deformation resistance at high applied stresses remains valid, as shown in this study.

1.7 Reasons for the enhanced creep performance in SX2 (SCM)-HT

Despite the similarities in creep behavior in the HT LPBFed-Ti6246, sample SX2 (SCM)-HT had the longest creep life. One reason might be the relatively stable microstructure (melt pool boundaries) observed in Figure 8(b). Indeed, the columnar microstructure of SX2 (SCM)-HT did not change or form any substructures except for the elongation of the α needles. From Figure 10, the α needles in SX2 (SCM)-HT showed the longest elongation. This suggests SX2 (SCM)-HT experienced the highest plastic deformation and the highest resistance to dislocation movements [34]. However, another possible explanation might lie beyond the sample's microstructure i.e. texture. Texture is a material property determinant known to influence creep significantly. As previously shown, the as-built texture in SX2 (SCM)-HT suggests that the crystallographic direction of the solidifying β-phase aligned in the <001> direction, parallel to the build direction and the applied external tensile stresses as presented in Figure 3 (b-1). This SCM texture perhaps accounts for the improved creep life performance. The <001> texture is the easy growth direction (preferential growth direction) of the body-centered cubic (bcc) β-phase and usually requires less energy for growth [35]. Moreover, the <001> direction possesses the least atom arrangements, resulting in the lowest elastic modulus [36]. Therefore, when high tensile stresses were applied to SX2 (SCM)-HT, the β-phase matrix was subjected to an increased strain owing to the smaller stiffness than that of the α needles [36]. The effect from the strained <001> matrix together with the ability of the α needles to hinder dislocation glide explains the observed improved creep life.

1.8 Creep voids formation, growth, and failure

In SX1 (CLM)-HT, SX2 (SCM)-HT, and SX3 (PCM)-HT, the melt pool and longitudinal boundaries constituted weak bonds. These weak bonds caused the nonuniform stress distribution at the boundaries during diffusional creep, leading to sliding and forming creep voids. As the applied stress increased, growth of the creep voids was driven by dislocation motion around the voids which ultimately resulted in the pull-out manifested as rings or shallow dimples, and the observed outlines of the laser scan pathways. The schematic presented in Figure 11 illustrates the creep voids initiation, and growth processes leading to fracture in the HT LPBFed Ti6246.

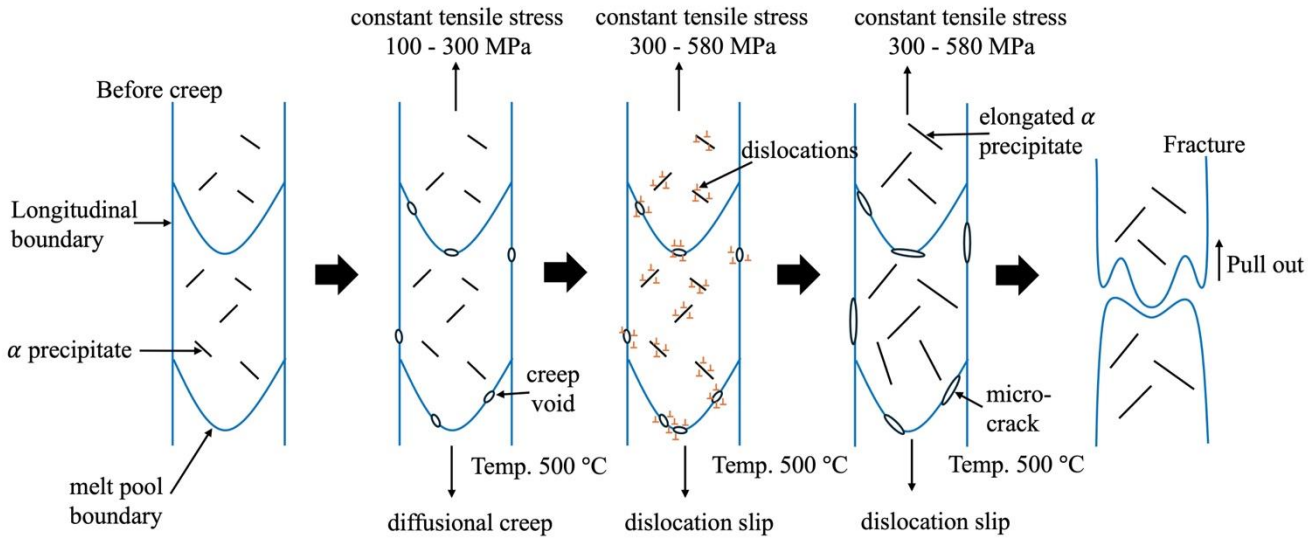

Figure 11: Schematic of creep voids formation, growth, and fracture of the HT LPBFed Ti6246.

Additionally, it is worth noting that the number of creep voids increased with the α-phase volume fraction in the respective samples, as evident in Figures 9 and 10. In all, the failure of the HT LPBFed-Ti6246 (SX1 (CLM)-HT, SX2 (SCM)-HT, and SX3 (PCM)-HT) was caused by the formation of creep voids that grew into microcracks at the melt pool boundaries (or grain boundaries) leading to intergranular fracture.

Conclusion

In this study, the microstructure, crystallographic texture, and high-temperature creep performance of Ti-6Al-2Sn-4Zr-6Mo wt.% (Ti6246) fabricated using three different LPBF process conditions (SX1 - 360 W, 800 mm/s; SX2 – 300 W, 1000 mm/s; SX3 – 180 W; 1200 mm/s) were investigated. Creep tests on the heat-treated (HT) LPBFed-Ti6246 were carried out at 500 °C. To understand occurring deformation mechanisms, the step creep test was first performed for each sample. The following conclusions were drawn:

- The as-built LPBFed-Ti6246 exhibited columnar microstructures but with three unique crystallographic textures. SX1 formed a crystallographic lamellar-like microstructure (CLM) texture while SX2 and SX3 formed the near <001> single crystal-like microstructure (SCM) and polycrystalline microstructure (PCM) texture, respectively.

- Heat treatment (HT) at 885 ° C provided sufficient energy and time for the α/α'martensitic phase to decompose to the α phase and grow. The α phases were located within the columnar structures and the melt pool boundaries of SX1 (CLM)-HT, SX2 (SCM)-HT, and SX3 (PCM)-HT.
- At low applied stresses (100 – 300 MPa), diffusional creep was the dominant deformation mechanism and its resistance depended on the grain size of the tested samples. The β-forged-HT, characterized by large equiaxed grains (138 ± 49 μm), exhibited the lowest strain rate compared to the columnar microstructure of SX1 (CLM)-HT, SX2 (SCM)-HT, and SX3 (PCM)-HT.
- Conversely, dislocation slip governed deformation at high applied stresses (400 - 580 MPa) and its efficacy depended on the α/β interfaces in the microstructures to impede dislocation mobility.
- The observed disjointed columnar grains in SX1 (CLM)-HT and the deformation of the polycrystalline grains in SX3 (PCM)-HT indicated that the melt pool boundaries were unstable in the LPBFed-Ti6246.
- Nonetheless, SX2 (SCM)-HT exhibited the longest creep life. Compared to SX1 (CLM)-HT and SX3 (PCM)-HT, SX2 (SCM)-HT maintained its continuous columnar structure till fracture. The relatively stable melt pool boundaries coupled with the near <001> SCM crystallographic texture of the β matrix in the build direction and parallel to the applied stresses culminated in an improved creep life compared to the reference β-forged-HT Ti6246.
- Shallow dimples, the observation of laser scan tracks, and cleavage facets characterized the fracture surfaces of the SX1 (CLM)-HT, SX2 (SCM)-HT, and SX3 (PCM)-HT. The failure mode in the SX1 (CLM)-HT, SX2 (SCM)-HT, and SX3 (PCM)-HT was by intergranular brittle fracture from forming creep voids, particularly at melt pool boundaries perpendicular to the applied tensile stresses.

In all, the present study showed that the LPBF process can usefully influence the microstructure and crystallographic texture of the Ti6246 alloy to attain enhanced properties. As evident in SX2 (SCM)-HT, forming a single crystal-like microstructure texture can improve

creep performance. In other words, this study reinforces the concept that crystallographic texture could be deliberately controlled using the LPBF process while simultaneously building parts with sophisticated geometries. This serves to benefit the aerospace industry in terms of saving time, energy, and cost in producing needed parts.

Declaration of Competing Interest

On behalf of all authors, the corresponding author states that there is no conflict of interest.

Acknowledgement

Special thanks to Mrs. Nina Kobata of NIMS for all her assistance during the creep tests.

Data availability

Data will be made available on request.

Funding

This work was supported by Grants-in-Aid for Transformative Research Area A [grant number JP21H05198] and for Scientific Research [grant number JP23H00235] from the Japan Society for the Promotion of Science (JSPS), and by The Light Metal Educational Foundation (Japan).

References

1. P. V. Cobbinah, R. A. Nzeukou, O. T. Onawale and W. R. Matizamhuka, Metals, 2020, 11, 58.
2. T. DebRoy, H. L. Wei, J. S. Zuback, T. Mukherjee, J. W. Elmer, J. O. Milewski, A. M. Beese, A. Wilson-Heid, A. De and W. Zhang, Progress in materials science, 2018, 92, 112-224.
3. A. Carrozza, A. Aversa, P. Fino and M. Lombardi, Journal of alloys and compounds, 2021, 870, 159329.
4. A. Carrozza, A. Aversa, P. Fino and M. Lombardi, Materials & design, 2022, 215, 110512.
5. H. Peng, S. Wu, W. H. Kan, S. C. V. Lim, Y. Zhu and A. Huang, Scripta Materialia, 2023, 226, 115209.
6. P. Yadav and K. K. Saxena, Materials Today: Proceedings, 2020, 26, 2546-2557.

7. C. Veiga, J. P. Davim and A. J. R. Loureiro, Rev. Adv. Mater. Sci, 2012, 32, 133-148.
8. P. V. Cobbinah, S. Matsunaga, Y. Toda, R. Ozasa, M. Okugawa, T. Ishimoto, Y. Liu, Y. Koizumi, P. Wang, T. Nakano and Y. Yamabe-Mitarai, Smart Materials in Manufacturing, 2024, 2, 100050.
9. K. Hagihara and T. Nakano, JOM, 2021, 1-14.
10. W. Shifeng, L. Shuai, W. Qingsong, C. Yan, Z. Sheng and S. Yusheng, Journal of Materials Processing Technology, 2014, 214, 2660-2667.
11. O. Gokcekaya, T. Ishimoto, S. Hibino, J. Yasutomi, T. Narushima and T. Nakano, Acta materialia, 2021, 212, 116876.
12. L. Thijs, M. L. Montero Sistiaga, R. Wauthle, Q. Xie, J.-P. Kruth and J. Van Humbeeck, Acta materialia, 2013, 61, 4657-4668.
13. O. Gokcekaya, N. Hayashi, T. Ishimoto, K. Ueda, T. Narushima and T. Nakano, Additive manufacturing, 2020, 36, 101624.
14. T. Ishimoto, S. Wu, Y. Ito, S.-H. Sun, H. Amano and T. Nakano, ISIJ international, 2020, 60, 1758-1764.
15. S. L. Corre, R. Forestier, F. Brisset, M. H. Mathon and D. Solas, in Proceedings of the 13th World Conference on Titanium, Wiley Online Library, 2016, pp. 757-764.
16. I. Weiss and S. L. Semiatin, Materials science & engineering. A, Structural materials : properties, microstructure and processing, 1998, 243, 46-65.
17. T. G. Langdon, Metallurgical and Materials Transactions A, 2002, 33, 249-259.
18. K. Sotoudeh and P. S. Bate, Acta Materialia, 2010, 58, 1909-1920.
19. C. Herring, Journal of Applied Physics, 1950, 21, 437-445.
20. Y. Yamabe-Mitarai, T. Inoue, T. Kuroda, S. Matsunaga, Y. Toda, T. Matsunaga, T. Ito, R. Ozasa, T. Ishimoto and T. Nakano, Materials Transactions, 2023, 64, 1175-1182.
21. E. Alabort, P. Kontis, D. Barba, K. Dragnevski and R. C. Reed, Acta Materialia, 2016, 105, 449-463.
22. K. R. Athul, U. T. S. Pillai, A. Srinivasan and B. C. Pai, Advanced Engineering Materials, 2016, 18, 770-794.
23. F. Appel, U. Lorenz, M. Oehring, U. Sparka and R. Wagner, Materials Science and Engineering: A, 1997, 233, 1-14.

24. T. Suzuki, S. Takeuchi and H. Yoshinaga, Dislocation dynamics and plasticity, Springer Science & Business Media, 2013.
25. F. A. Mohamed and T. G. Langdon, Acta metallurgica, 1974, 22, 779-788.
26. Y. He, Y. e. Ma, W. Zhang and Z. Wang, Engineering Failure Analysis, 2022, 135, 106063.
27. G. Malakondaiah and R. Rao, Defence Science Journal, 1985, 35, 201-217.
28. Z. H. Xiong, S. L. Liu, S. F. Li, Y. Shi, Y. F. Yang and R. D. K. Misra, Materials Science and Engineering: A, 2019, 740-741, 148-156.
29. P. C. Millett, T. Desai, V. Yamakov and D. Wolf, Acta Materialia, 2008, 56, 3688-3698.
30. J. E. Harris, Metal Science Journal, 1973, 7, 1-6.
31. W. Huang and Y. Zhang, Journal of Manufacturing Processes, 2019, 42, 139-148.
32. J. Sun, X. Zhu, L. Qiu, F. Wang, Y. Yang and L. Guo, Materials Today Communications, 2019, 19, 277-285.
33. Y. Ro, S. Nakazawa, H. Onodera, K. Ohno, T. Yamagata, I. Tomizuka and M. Yamazaki, ISIJ International, 1989, 29, 165-170.
34. R. Ullah, J. Lu, L. Sang, Y. Xiaoxiao, W. Zhang, Y. Zhang and Z. Zhang, Journal of Alloys and Compounds, 2020, 817, 152781.
35. T. Ishimoto, K. Hagihara, K. Hisamoto, S.-H. Sun and T. Nakano, Scripta Materialia, 2017, 132, 34-38.
36. S. G. Tian, H. H. Zhou, J. H. Zhang, H. C. Yang, Y. B. Xu and Z. Q. Hu, Materials Science and Technology, 2000, 16, 451-456.